INORGANIC CHEMISTRY FRONTIERS

RESEARCH ARTICLE

View Article Online
View Journal | View Issue

Cite this: *Inorg. Chem. Front.*, 2024, **11**, 2784

Achieving high-sensitivity dual-mode optical thermometry *via* phonon-assisted cross-relaxation in a double-perovskite structured up-conversion phosphor†

Houhe Dong,‡[a] Zonghao Lei,‡[a] Shikun Su,[a] Wenhua Yang,*[a] Xuyang Zhang,[a] Wenying Teng,[a] Guangyue Zu,[a] Bing Teng*[a,b] and Degao Zhong *[a,b,c]

Received 10th February 2024,
Accepted 3rd April 2024

DOI: 10.1039/d4qi00395k

rsc.li/frontiers-inorganic

High sensitivity is still a challenge for achieving optical thermometry applications. In this work, we effectively regulated the phonon energy of matrix crystals by substituting the A-site ions in the tellurate double perovskite up-conversion (UC) phosphors of $ALaLiTeO_6$:5%Yb^{3+},0.2%Tm^{3+} with Ca^{2+}, Sr^{2+}, and Ba^{2+}. On this basis, a dual-mode thermometer based on the fluorescence intensity ratio of $FIR_1 = I_{694}/I_{649}$ and $FIR_2 = I_{694}/I_{475}$ was constructed by utilizing significant differences in the response to temperature changes between 649 nm/475 nm emissions (from both Yb^{3+} and Tm^{3+}) and 694 nm UC emission (from $Yb^{3+} \rightarrow Tm^{3+}$). As the temperature increases, involving the assistance of matrix crystal phonon energy, the collaborative action of two non-radiative transitions (Tm^{3+}) and three cross-relaxation processes (Tm^{3+}–Tm^{3+}) can degrade the emission intensity at 475 and 649 nm, but enhance the UC emission intensity at 694 nm, thus effectively improving the thermometry sensitivity. Finally, we achieved the maximum thermometry sensitivity values of $S_r = 4.69\%\ K^{-1}$ and $S_a = 10.05\%\ K^{-1}$. These results provide new insights into exploring and constructing ultra-sensitive optical temperature sensors.

1. Introduction

Optical thermometry uses temperature-sensitive parameters such as the luminescence wavelength, intensity, lifetime, and fluorescence intensity ratio (FIR) of fluorescent substances to achieve temperature measurement.[1–3] Among them, FIR-based thermometry has become a widely used temperature measurement technology solution due to its advantages such as fast response speed and a wide temperature measurement range.[4–6] FIR technology can be implemented in two ways: thermal coupling level (TCL) and non-thermal coupling level (NTCL).[7,8] However, since the energy gap (ΔE) of the TCL is limited to a range of 200–2000 cm^{-1}, it is difficult to obtain high relative sensitivity because it is proportional to ΔE ($S_r = \Delta E/kT^2$).[9,10] Hence, there is substantial practical merit in the design and development of advanced optical thermometers characterized by high sensitivity across a broad temperature range, leveraging the NTCL of luminescent ions.[11–13]

For UC luminescent materials used in optical thermometry, high-quality matrix crystals are one of the key elements to achieve accurate and efficient optical thermometers.[14–18] Fluoride matrix crystals (such as $NaYF_4$, SrF_2, LuF_3, *etc.*) normally exhibit efficient UC luminescence due to their low phonon energy.[19–21] However, their production processes are complex and their poor thermal stability can induce the degradation of luminescence properties under harsh conditions. Oxide matrix crystals such as titanate, molybdate and tellurate not only maintain excellent chemical structure stability at high temperatures, but also have suitable phonon energies, which can provide various crystal field environments for rare earth luminescent ions, making them ideal UC luminescent matrix crystals.[22–27] Among them, the recently developed tellurate double perovskite structure has multiple cation sites that can be selectively occupied by luminescent ions, providing multiple options for regulating luminescence performance and thermometric energy level pair screening. In particular, the double perovskite structure of $ALaLiTeO_6$ (A = Ca, Sr, and Ba) has received widespread attention as a matrix for luminescent materials.[28–30] In 2014, S. K. Sali *et al.* for the first time synthesized a double perovskite-type compound $BaA'LaTeO_6$ (A′ =

---

[a] *College of Physics, University-Industry Joint Center for Ocean Observation and Broadband Communication, Qingdao University, Qingdao 266071, China. E-mail: yangwh@qdu.edu.cn, 5108tb@163.com, zhdg2008@126.com*

[b] *Qingdao Broadband Terahertz Spectroscopy Technology Engineering Research Center, Qingdao University, Qingdao 266071, China*

[c] *Weihai Innovation Research Institute of Qingdao University, Weihai 264200, China*

† Electronic supplementary information (ESI) available. See DOI: **https://doi.org/10.1039/d4qi00395k**

‡ These authors contributed equally to this work.

Na, K, and Rb) and determined its crystal structure using Rietveld analysis and neutron diffraction data.[31] In 2017, G. Subodh *et al.* synthesized the B-site ordered double perovskite $ALaLiTeO_6$ (A = Ba and Sr) and investigated the vibrating phonon modes for the first time.[32] In 2021, Subodh Ganesanpotti *et al.* investigated the application of an Mn^{4+}-activated $SrLaLiTeO_6$ crimson phosphor in indoor plant growth LEDs. The redshift of the high-energy phonon mode in Raman spectroscopy and infrared spectroscopy confirmed the B-site substitution of Mn^{4+} ions.[33] In 2023, Dai *et al.* proved that $SrLaLiTeO_6$:Eu/Dy were potential candidate phosphors for indoor plant growth LEDs and pc-wLEDs.[34] In the same year, Zhang *et al.* prepared an Er^{3+} doped $ALaLiTeO_6$ (A = Ba, Sr, Ca and Mg) phosphor and revealed its excellent temperature measurement performance. Previous studies have confirmed that $ALaLiTeO_6$ is an excellent matrix crystal.[35] However, as far as we know, research on the UC phosphors of $ALaLiTeO_6$ (A = Ca, Sr, and Ba) doped with Yb^{3+} and Tm^{3+} has not been reported and its application potential in optical thermometry urgently needs to be explored and evaluated.

In this work, UC phosphors of $ALaLiTeO_6:Yb^{3+},Tm^{3+}$ (A = Ca, Sr, and Ba) were synthesized through the high-temperature solid-state method. The characteristics of the crystal structure were analyzed in detail through first-principles calculations and X-ray diffraction. The temperature-dependent UC emission spectra were measured. With the increase of temperature, phonon-assisted cross-relaxation processes gradually play dominant roles in determining the emission intensities at 475, 649 and 694 nm. The maximum thermometry sensitivities of S_r = 4.69% K^{-1} (303 K) and S_a = 10.05% K^{-1} (693 K) were achieved from the constructed dual-mode thermometer based on the fluorescence intensity ratios of $FIR_1 = I_{694}/I_{649}$ and $FIR_2 = I_{694}/I_{475}$. The application potential of $ALaLiTeO_6$:5%Yb^{3+},0.2%Tm^{3+} in temperature sensing is evaluated.

2. Experimental

2.1 Materials synthesis

All samples of $ALaLiTeO_6:Yb^{3+},Tm^{3+}$ (A = Ca, Sr, and Ba) were synthesized using the high-temperature solid-state method. Firstly, the initial reaction compounds (purchased from Aladdin) of $CaCO_3$ (99.9%), $SrCO_3$ (99.9%), $BaCO_3$ (99.9%), La_2O_3 (99.99%), Li_2CO_3 (99.99%), TeO_2 (99.9%), Yb_2O_3 (99.99%), and Tm_2O_3 (99.99%) were weighed according to the stoichiometric ratio. Secondly, the starting materials were thoroughly mixed in an agate mortar and ground for 30 minutes. Thirdly, the ground mixture was pre-sintered at 600 °C for 6 hours, and then the samples were sintered at 1000 °C for 4 hours. Finally, the samples were cooled to room temperature and ground into powder for subsequent structural and optical performance testing.

2.2 Characterization

The phase structure of the phosphor $ALaLiTeO_6:Yb^{3+},Tm^{3+}$ (A = Ca, Sr, and Ba) was tested using a Rigaku Ultima IV X-Ray diffractometer (XRD) equipped with Cu-Kα radiation (λ = 1.5418 Å) and the scan rate was 5° min^{-1} at 40 kV and 40 mA. The morphology was obtained using a scanning electron microscope (JSM-7800F), and the elemental distribution was analyzed by an energy dispersive spectrometer (EDS) detector. An X-ray photoelectron spectrometer (PHI5000) was employed to collect X-ray photoelectron spectroscopy (XPS) spectra of the $ALaLiTeO_6:Yb^{3+},Tm^{3+}$ samples so as to determine their composition and elemental valence states. Raman spectroscopy was performed using a laser Raman spectrometer (WITEC 300) with a laser wavelength of 532 nm. In the measurement, the power was set at 3.5 mW in order to minimize the heat effect of the laser.

A power tunable 980 nm laser was selected as the UC luminescence excitation source, and an Edinburgh FS5 fluorescence spectrometer was used to test the photoluminescence spectra (PL), and temperature-dependent luminescence spectra. The test was repeated more than three times in an effort to ensure the accuracy of the data. The spectral step of the PL spectra was set as 1.0 nm, and the slit width of the monochromator was set as 0.3 nm. Temperature-dependent PL spectra spanning from 303 to 693 K were obtained through a temperature-controlled platform (INSTEC, MK2000 and HCP621G-CUV1) integrated with an FS5 fluorescence spectrometer. All measurements were conducted at room temperature, except the temperature dependent PL spectra.

3. Results and discussion

3.1 Crystal structure and phase identification

Previous studies have confirmed that $CaLaLiTeO_6$ and $SrLaLiTeO_6$ have monoclinic phases ($P2_1/n$), while $BaLaLiO_6$ possesses a cubic phase structure ($Fm\bar{3}m$). In this work, the measured XRD patterns of the synthesized non-doped and Yb^{3+}, Tm^{3+} co-doped $ALaLiTeO_6$ samples are shown in Fig. 1a. The XRD diffraction patterns of $ALaLiTeO_6$:5%Yb^{3+},0.2%Tm^{3+} are consistent with those of the corresponding standard CIF cards, indicating that the co-doping with Yb^{3+} and Tm^{3+} does not cause serious structural distortions in the double-perovskite.

In order to further validate the crystal structure of $ALaLiTeO_6$:5%Yb^{3+},0.2%Tm^{3+} (A = Ca, Sr, and Ba), we respectively utilized standard structures of PDF # 04-018-0711, PDF # 04-018-0713, and ICSD # 67851 as the initial data to conduct Rietveld structure refinement of $ALaLiTeO_6$:5%Yb^{3+},0.2%Tm^{3+} (A = Ca, Sr, and Ba) using the GSAS II program. As shown in Fig. 2a and Table S1–S3,† the refinement results showed that all samples' data were well fitted, and they all converge to low reliability factors, indicating good consistency between the experimental data and the standard structure. Due to the substitution of Ba^{2+}, Sr^{2+}, and Ca^{2+} in the A-site, $ALaLiTeO_6$ undergoes a phase transformation from $BaLaLiO_6$ with a cubic phase ($Fm\bar{3}m$) to $CaLaLiTeO_6$ and $SrLaLiTeO_6$ with a monoclinic phase ($P2_1/n$). Accompanied by structural phase transformation, the cell volumes of $BaLaLiTeO_6$ (5% Yb^{3+},0.2% Tm^{3+}), $SrLaLiTeO_6$ (5% Yb^{3+}, 0.2% Tm^{3+}), and $CaLaLiTeO_6$ (5% Yb^{3+},

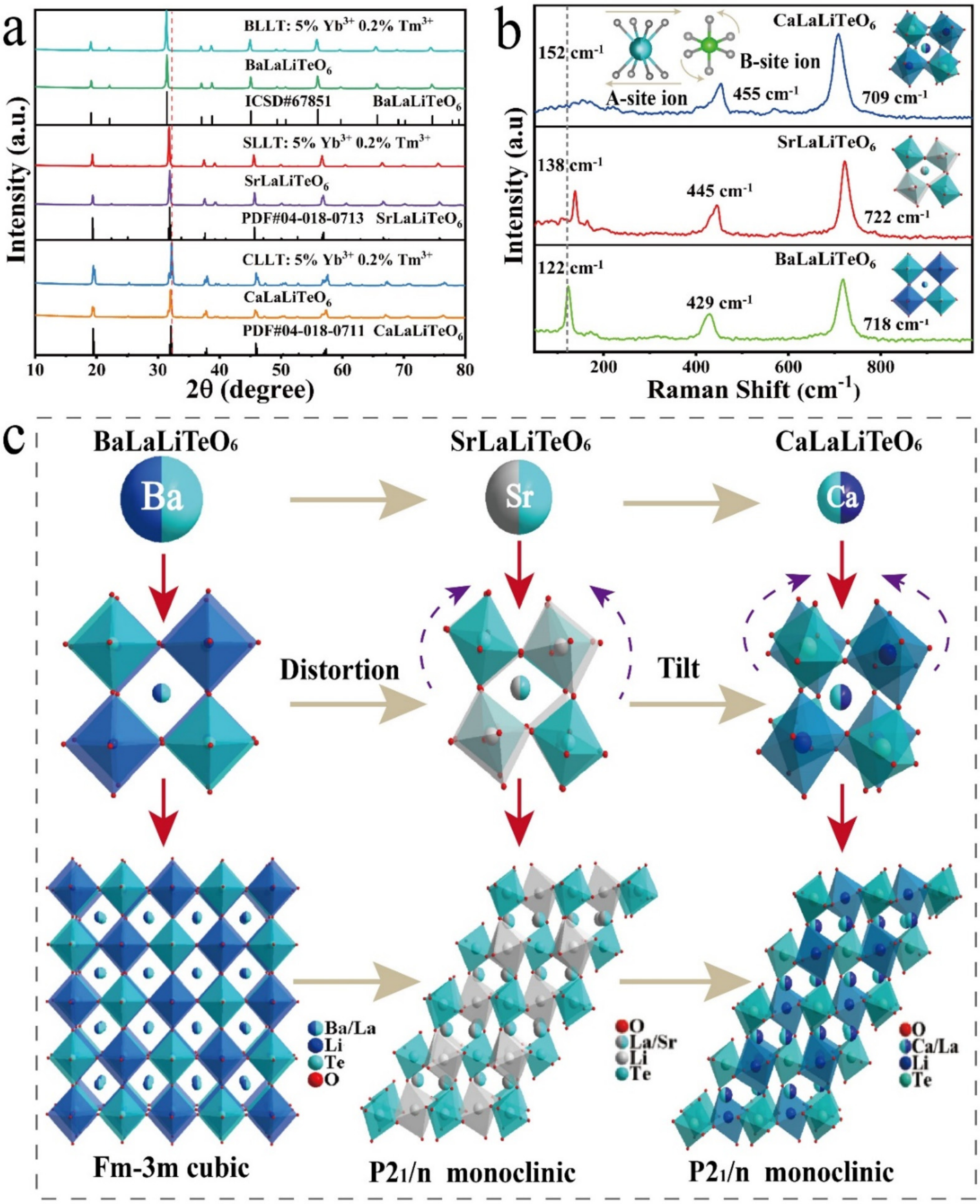

Fig. 1 (a) XRD patterns of the non-doped and 5% Yb^{3+}, 0.2% Tm^{3+} co-doped $ALaLiTeO_6$ (A = Ca, Sr and Ba). (b) Raman spectra and (c) crystal structure of $ALaLiTeO_6$ (A = Ca, Sr and Ba).

0.2% Tm^{3+}) gradually shrink from 526.272 $Å^3$ to 251.83 $Å^3$ and 245.884 $Å^3$.

In order to probe into the possible lattice occupation of Yb^{3+} and Tm^{3+} in $ALaLiTeO_6$, we calculated the radius differences induced by substitutions of (Yb^{3+},Tm^{3+}) → La^{3+} and (Yb^{3+},Tm^{3+}) → A(Ca^{2+}, Sr^{2+}, Ba^{2+}) using the following formula:[36–38]

$$D_r = \frac{R_S - R_D}{R_S} \times 100\% \tag{1}$$

where R_S and R_D represent the radius of the substituted ions (La^{3+}, Ca^{2+}, Sr^{2+}, and Ba^{2+}) and doped ions (Yb^{3+} and Tm^{3+}), respectively. The calculated results are summarized in Table S4.† As listed in Table S4,† the D_r values for the replacement of (Yb^{3+}, Tm^{3+}) → La^{3+} are 15.1% and 14.3%, respectively, which are less than 30%. Taking into account the small radius difference and the fact that there is no charge difference between La^{3+} and (Yb^{3+}, Tm^{3+}), we speculate that Yb^{3+} and Tm^{3+} are more likely to occupy the lattice sites of La^{3+}.

As shown in Fig. 1c, the skeleton structure of $ALaLiTeO_6$ is composed of alternating and co-angular B(B′) octahedron [TeO_6] and [LiO_6], while the A(A′) site ions with coordination number of CN = 8 are filled in the gaps between the alternating octahedra to balance the entire charge and maintain struc-

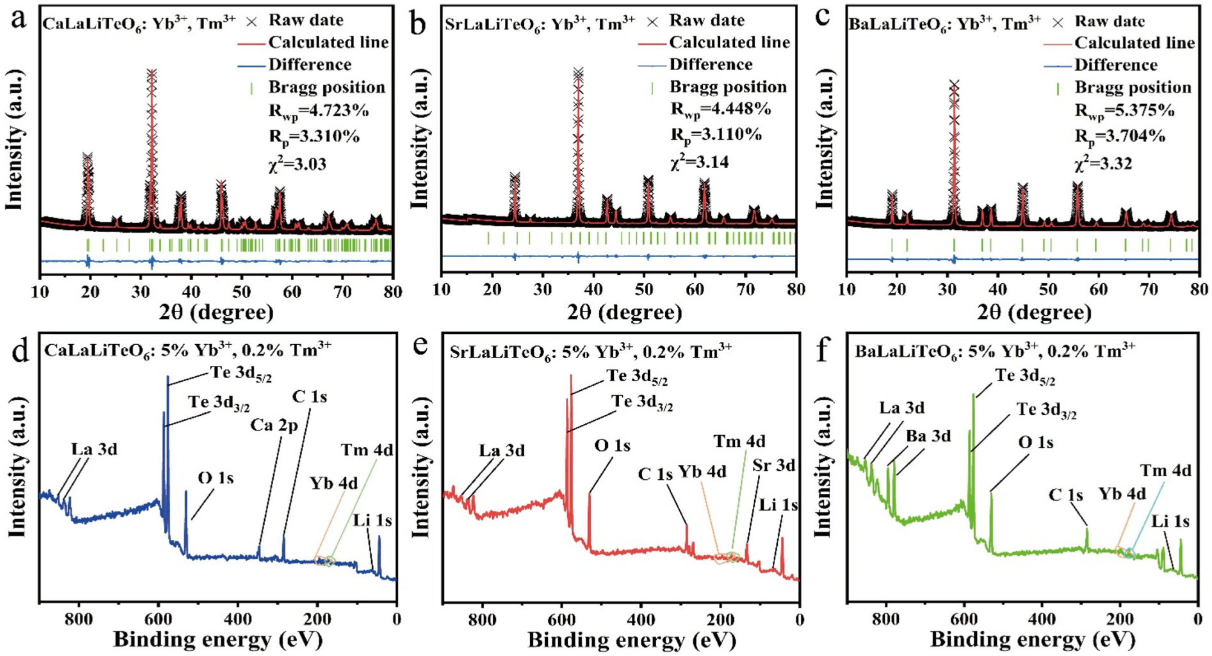

Fig. 2 XRD refined picture of (a) $CaLaLiTeO_6$:5%Yb^{3+},0.2%Tm^{3+}, (b) $SrLaLiTeO_6$:5%Yb^{3+},0.2%Tm^{3+}, and (c) $BaLaLiTeO_6$:5%Yb^{3+},0.2%Tm^{3+}. XPS spectra of (d) $CaLaLiTeO_6$:5%Yb^{3+},0.2%Tm^{3+}, (e) $SrLaLiTeO_6$:5%Yb^{3+},0.2%Tm^{3+}, and (f) $BaLaLiTeO_6$:5%Yb^{3+},0.2%Tm^{3+}.

tural stability. Due to different radii of alkali metal ions occupying the A(A′) sites, the distortion and tilt of the octahedra of $[TeO_6]$ and $[LiO_6]$ will degrade the structural symmetry from the $Fm\bar{3}m$ cubic phase to the $P2_1/n$ monoclinic phase. The distortion of the perovskite depends on the size and interaction of the A-site cation and the corner-sharing $B(B')O_6$ octahedra. The Goldschmidt tolerance factor (σ) is a reliable empirical index to analyze the size mismatch between the A-site cation and the $[B(B')O_6]$ octahedra, which can be calculated using the following expression:[30]

$$\sigma = \frac{r_A + r_O}{\sqrt{2}\left(\frac{r_{Li} + r_{Te}}{2} + r_O\right)} \tag{2}$$

where r_A, r_{Li}, r_{Te}, and r_O are the radii of $A^{2+}(A'^{3+})$, Li^+, Te^{6+} and O^{2-}, respectively. In double-perovskite $ALaLiTeO_6$, A^{2+}, La^{3+}, Yb^{3+} and Tm^{3+} cations are mixed in the A site, and thus r_A is the weighted average ionic radii of different cations. The calculated σ values for $ALaLiTeO_6$:5%Yb^{3+},0.2%Tm^3 crystals are 0.920(A = Ba), 0.894(A = Sr), and 0.871(A = Ca), respectively. Therefore, the perovskite structure becomes more distorted with the decreasing ionic radii of A^{2+} cations. With the substitution of Ba^{2+}, Sr^{2+}, and Ca^{2+} cations, the local symmetry of La (Yb^{3+}, Tm^{3+}) sites will also change, resulting in lattice distortion and contraction, which can affect thermal stability of crystal field environments around luminescent ions.

Raman peaks are caused by lattice vibrations, and the Raman peak position and intensity represent the distribution of phonon energy. Raman spectroscopy can analyze changes in the vibration mode and further identify the effect of A-position substitution on phonon energy. Fig. 1b shows the measured Raman spectra of $ALaLiTeO_6$ at λ_{ex} = 532 nm. With the replacement of Ca^{2+}, Sr^{2+}, and Ba^{2+} cations, the Raman intensity located at 100–230 cm^{-1} corresponding to the translation vibration of the A position cations is red-shifted and its peak intensity increases. The Raman peaks located at 400–470 cm^{-1} corresponding to the flexion vibration of the B-site cationic oxygen octahedron are also blue-shifted. The strong mode centered at 700–730 cm^{-1} corresponds to symmetric stretching vibrations of the lattice.[32–34] $ALaLiTeO_6$ has strong Raman peaks at 100–230 cm^{-1}, 400–470 cm^{-1} and 700–730 cm^{-1}, and the substitution of A-site ions induces a great influence on the position and intensity of Raman peaks, that is, on phonon energy.

The SEM images of the synthesized $ALaLiTeO_6$:5% Yb^{3+},0.2%Tm^{3+} samples are illustrated in Fig. S2.† The morphology of the samples exhibits an irregular polyhedral shape, with grain sizes ranging from several micrometers to hundreds of nanometers. EDS measurements indicate that Ca, Sr, Ba, La, Te, O, Yb, and Tm elements were evenly distributed in the phosphor particles. Element lithium has a low atomic number, which is beyond the detection range, so it could not be detected. However, the subsequent XPS testing proves that lithium had been doped into $ALaLiTeO_6$. The measured XPS spectra of $ALaLiTeO_6$:5%Yb^{3+},0.2%Tm^{3+} samples are shown in Fig. 2. All elements in the experimental synthesis were detected in the XPS spectra, including Ca^{2+}, Sr^{2+}, Ba^{2+}, La^{3+}, Li^+, Te^{6+}, O^{2-}, Yb^{3+}, and Tm^{3+}. The Te-3d core spectra assigned Te-$3d_{5/2}$ and Te-$3d_{3/2}$ peaks at 575 and 586 eV are characteristics of Te^{6+} and hence, imply the complete oxidation of the

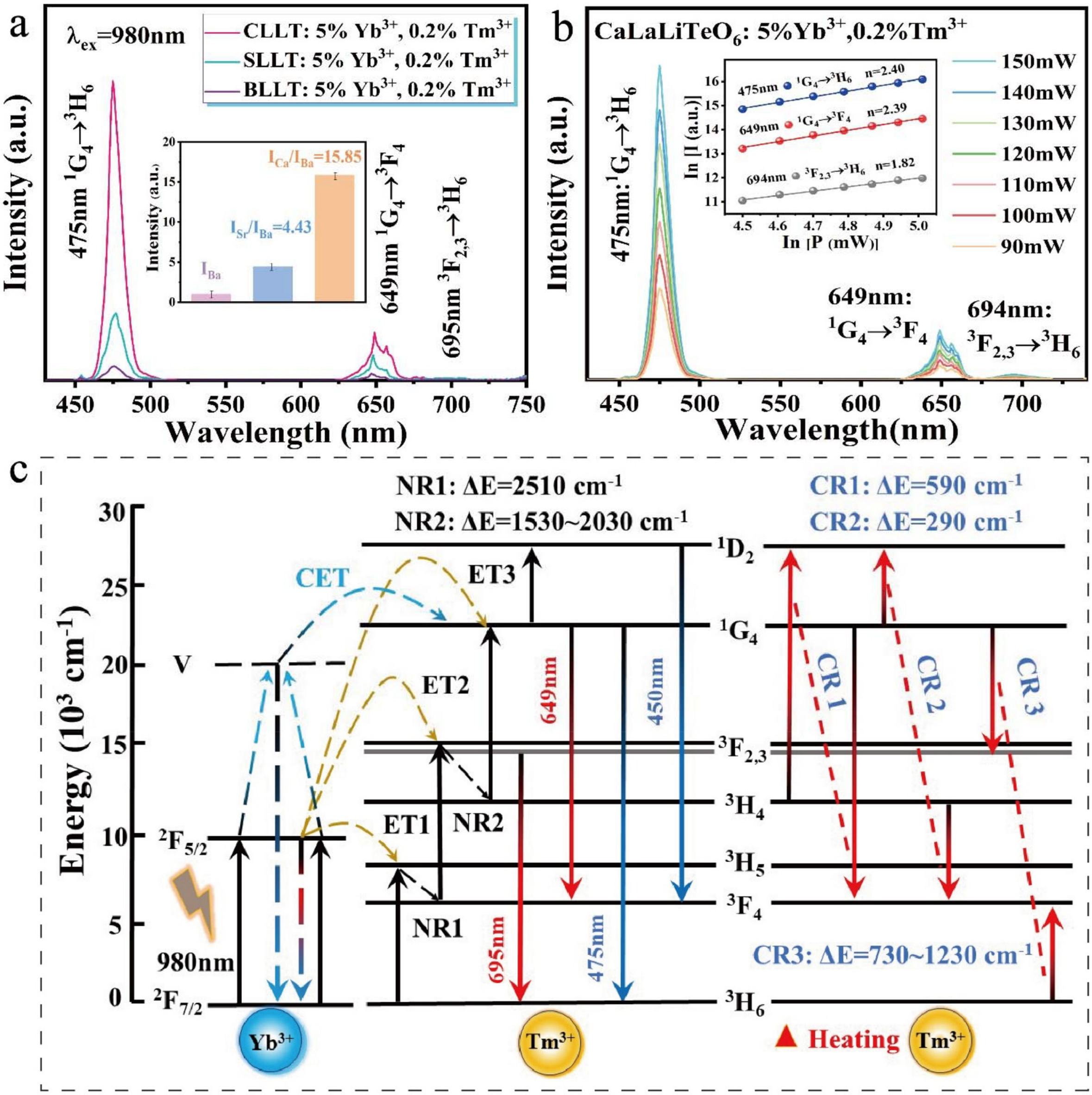

Fig. 3 (a) Up-conversion PL spectra of $ALaLiTeO_6$:5%Yb^{3+},0.2%Tm^{3+} (A = Ca, Sr, and Ba). (b) The relationship between ln(I) and ln(P) of $CaLaLiTeO_6$:5%Yb^{3+},0.2%Tm^{3+}. (c) Energy level diagram and thermally enhanced CR processes in the $ALaLiTeO_6$:5%Yb^{3+},0.2%Tm^{3+} phosphor.

Te ion in the matrix. In short, the above results indicate that we have successfully synthesized the samples $ALaLiTeO_6$:5% Yb^{3+},0.2%Tm^{3+}.

3.2 Up-conversion luminescence properties and mechanism of $ALaLiTeO_6$:Yb^{3+},Tm^{3+}

As shown in Fig. S3,† the optimal doping concentration of $CaLaLiTeO_6$ is determined to be 5%Yb^{3+} and0.2%Tm^{3+}. The PL spectra of $ALaLiTeO_6$:5%Yb^{3+},0.2%Tm^{3+} are shown in Fig. 3a. Under excitation of a 980 nm laser, all samples demonstrate the same characteristic emission peaks of Tm^{3+} ions (475 nm: $^1G_4 \rightarrow {}^3H_6$; 649 nm: $^1G_4 \rightarrow {}^3F_4$; 694 nm: $^3F_{2,3} \rightarrow {}^3H_6$).[39,40] It is worth noting that, as shown in Fig. 3c and Fig. S4,† the cooperative energy transfer (CET) mechanism exists in the $ALaLiTeO_6$ (A = Ca, Sr, and Ba) samples with single-doped Yb^{3+} ions and double-doped Yb^{3+}, Tm^{3+} ions. Two Yb^{3+} ions in the ground state $^2F_{7/2}$ are simultaneously excited to the $^2F_{5/2}$ level after absorbing two 980 nm photons. In the excitation energy level, part of Yb^{3+} ions further increase to the virtual energy level, and then transition from the virtual energy level to the ground state energy level $^2F_{7/2}$ and emit light at 475 nm. The Tm^{3+} ions in the $^3H_6$ low level can be directly excited to the $^1G_4$ level after receiving the energy transferred from the Yb^{3+} ions in the virtual energy level.[41,42] Another part of Yb^{3+} ions at the excitation energy level $^2F_{5/2}$ can undergo an energy transfer process with Tm^{3+}. Under 980 nm excitation, Yb^{3+} ions undergo a transition of $^2F_{7/2}$ + *hν* (980 nm) → $^2F_{5/2}$, followed by an energy transfer (ET) process

ET1 and resulting in Tm^{3+} ions to be excited from the $^3H_6$ level to the $^3H_5$ level. Next, with the completion of the non-radiative (NR) transition process from the $^3H_5$ level to the $^3F_4$ level ($\Delta E \approx 2500\ cm^{-1}$), the ET2 process will occur: $^3F_4(Tm^{3+})$ + $^2F_{5/2}(Yb^{3+}) \rightarrow {}^3F_{2,3}(Tm^{3+})$ + $^2F_{7/2}$ (Yb^{3+}), the two-photon transition from $^3F_{2,3} \rightarrow {}^3H_6$ results in the emission of deep red (694 nm) emissions. Finally, accompanied by the completion of the $^3F_{2,3} \rightarrow {}^3H_4$ NR transition process ($\Delta E \approx$ 1530–2030 cm^{-1}), the ET3 process occurred: $^3H_4$ (Tm^{3+}) + $^2F_{5/2}(Yb^{3+}) \rightarrow {}^1G_4(Tm^{3+})$ + $^2F_{7/2}$ (Yb^{3+}). Strong blue (475 nm) and red (649 nm) emissions can be achieved by the three-photon transitions of $^1G_4 \rightarrow {}^3H_6$ and $^1G_4 \rightarrow {}^3F_4$, respectively. Remarkably, there is also a four-photon process taking place: $^1G_4(Tm^{3+})$ + $^2F_{5/2}(Yb^{3+}) \rightarrow {}^1D_2(Tm^{3+})$ + $^2F_{7/2}$ (Yb^{3+}), the $^1D_2 \rightarrow {}^3F_4$ transition process results in a weak blue light (450 nm) emission.[40,43–45]

In order to elucidate the UC luminescence mechanism of Yb^{3+} and Tm^{3+} co-doped $ALaLiTeO_6$ phosphors, the UC emission spectra of $ALaLiTeO_6$:5%Yb^{3+},0.2% Tm^{3+} phosphors were measured at different laser pump powers. The relationship between UC luminescence intensity (I) and laser power (P) from the excitation source can be fitted through the following equation:[43]

$$I \propto P^n \tag{3}$$

where n represents the exact number of photons involved in the UC process. By taking logarithmic functions on both sides of eqn (3), the functional relationship curve between ln (I) and ln (P) can be obtained, as shown in Fig. 3b and Fig. S5.† By linear fitting, the corresponding power exponents (n) of the emission at 475 nm, 649 nm and 694 nm in $CaLaLiTeO_6$:5% Yb^{3+},0.2%Tm^{3+} are 2.40, 2.39 and 1.82, respectively. The calculated value of n for these luminous transitions is almost equal to 2, indicating that $^1G_4 \rightarrow {}^3H_6$ and $^1G_4 \rightarrow {}^3F_4$ are mainly two-photon absorption processes with a small amount of three-photon absorption processes, this may be because the CET process of Yb^{3+} ions involved in UC luminescence is a two-photon process. The calculated n value of $^3F_{2,3} \rightarrow {}^3H_6$ is 1.82, which indicates a two-photon absorption process. Yb^{3+} and Tm^{3+} co-doped $SrLaLiTeO_6$ and $BaLaLiTeO_6$ phosphors exhibit the same UC photon absorption characteristics as $CaLaLiTeO_6$.

As demonstrated in Fig. 3a, it is worth noting that the emission intensity of $ALaLiTeO_6$:5%Yb^{3+},0.2%Tm^{3+} exhibits significant changes with different types of A-site occupying ions. Specifically speaking, the emission intensity of $CaLaLiTeO_6$:5%Yb^{3+}, 0.2% Tm^{3+} is 15.85 times stronger than that of $BaLaLiTeO_6$:5%Yb^{3+},0.2%Tm^{3+}. Therefore, in the Yb^{3+} and Tm^{3+} co-doped $ALaLiTeO_6$ system, the size of the A-site cation has a significant impact on the photoluminescence performance of the phosphor. However, the probability of a radiation transition from $^3F_{2,3}$ to $^3H_6$ occurring at room temperature is still very small, because the 694 nm intense red-light emission corresponding to this transition was observed to be weak in the measured emission spectrum. Based on the FT-IR and Raman spectroscopy test results shown in ESI Fig. S6,† the strongest cutoff band phonon frequencies generated by stretching vibration in the crystal are located at 650 cm^{-1} and 720 cm^{-1}, respectively, indicating that the maximum phonon energy distribution in the crystal is in the range of 650–720 cm^{-1}. At room temperature, Tm^{3+} ions tend to decay from level-$^3F_{2,3}$ to level-$^3H_4$ with the assistance of 2–3 phonons, as the non-radiative transition of $^3F_{2,3} \rightarrow {}^3H_4$ only need to span an energy interval of 1530–2030 cm^{-1}. With the increase of temperature, the phonon-assisted cross relaxation process of Tm^{3+}–Tm^{3+} gradually plays a dominant role in UC luminescence, and the transition probability of $^3F_{2,3} \rightarrow {}^3H_6$ gradually increases. This will be discussed further in section 3.4.

3.3 First principles calculations

In order to further explore the changes in the crystal structure and luminescence properties caused by the substitution of basic metals Ca, Sr and Ba in the $ALaLiTeO_6$ system, we performed first-principles calculations of the system. All density functional theory (DFT) calculations for structure optimization energies, and band structures were implemented in the Cambridge Serial Total Energy Package (CASTEP) with the ultrasoft pseudopotentials (USPs). The generalized gradient approximation (GGA) using Perdew–Burke–Ernzerhof (PBE) functional was adopted to treat the exchange and correlation energy. The electronic band structures and density of states of the $ALaLiTeO_6$ (A = Ca, Sr, and Ba) and the Yb, Tm-doped $ALaLiTeO_6$:Yb,Tm (A = Ca, Sr, and Ba) were calculated by using the first-principles calculation based on density functional theory. The initial crystal configuration of $ALaLiTeO_6$ (A = Ca, Sr, and Ba) was constructed according to the experimental results reported by M. L. Veiga *et al.*[46] The 2 × 2 × 1 and 2 × 1 × 1 supercells of $ALaLiTeO_6$ (A = Ca, Sr, and Ba) that have 80 atoms were constructed for the DFT calculation in this work. The plane-wave cutoff energy was set to 450 eV to ensure accuracy. An appropriate Monkhorst–Pack Brillouin sampling grid with a spacing of $2\pi \times 0.04\ A^{-1}$ was used for all structures. The convergence criterion of optimization for the total energy and force on the atoms, were 0.02 meV per atom and 0.05 eV Å^{-1}.

To examine the influence of ion doping on the electronic structure, the electronic band structure and the density-of-states of the $ALaLiTeO_6$ (A = Ca, Sr, and Ba) matrix, Yb doped and Yb, Tm-doped $ALaLiTeO_6$ (A = Ca, Sr, and Ba) were calculated based on density functional theory (DFT). As shown in Fig. 4 and Fig. S7,† the monoclinic structures $CaLaLiTeO_6$ and $SrLaLiTeO_6$ have indirect band gaps of 2.567 eV and 2.515 eV, respectively. After Yb ion doping, the sample changes from an indirect band gap to a direct band gap, and the band gap value decreases significantly, which is beneficial for the excitation of electrons. With co-doping Yb and Tm ions, the direct band gap decreases to 2.161 eV and 2.251 eV located in the Brillouin zone at the same G symmetry point in the region, it can be seen that the band gap change of $CaLaLiTeO_6$ is the most obvious. Due to its minimum band gap value, it can be concluded that the transition of electrons from the valence band to the conduction band is more likely to occur, and in

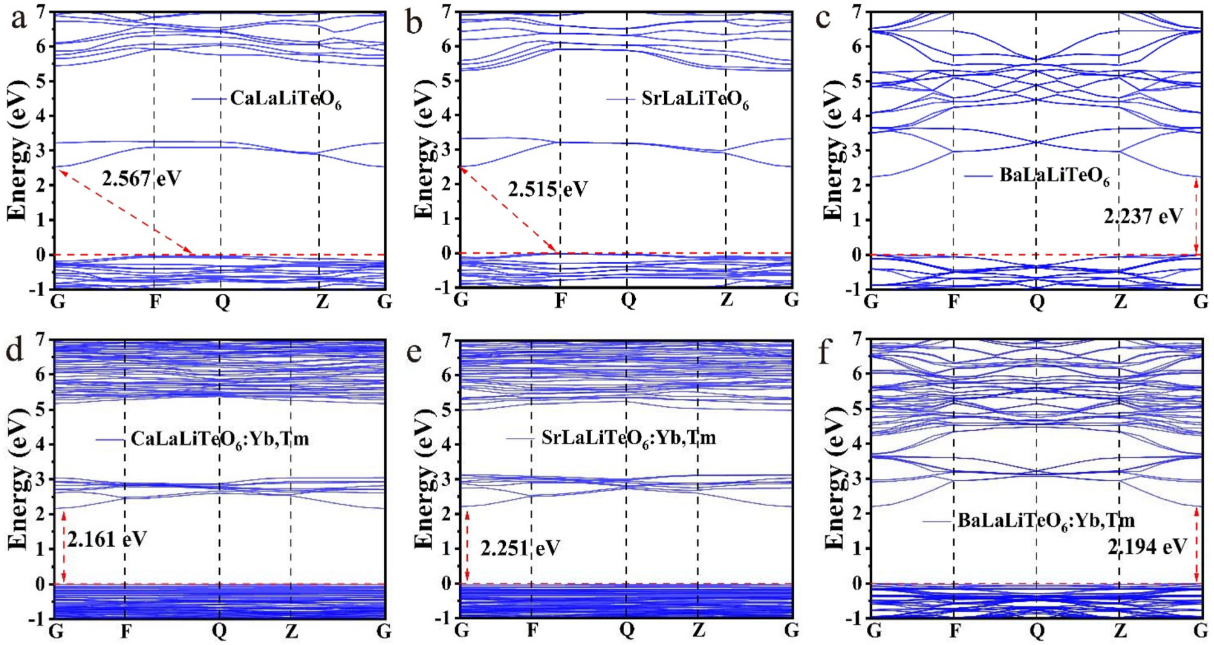

Fig. 4 Calculated band structures of (a–c) $ALaLiTeO_6$ and (d–f) $ALaLiTeO_6$:Yb,Tm with (A = Ca, Sr, and Ba).

the best $CaLaLiTeO_6$ system the luminous intensities confirm each other. The band gap change of the cubic structure $BaLaLiTeO_6$ is different from that of the monoclinic structure, its direct band gap is 2.237 eV. With the doping of Yb and Tm ions, the sample still has a direct band gap (2.241 eV and 2.194 eV). In addition, we also tested the UV-Vis diffuse reflectance spectra of the samples, and calculated the band gap values corresponding to each sample using the Wood–Tauc (W–T) formula and the Kubelka–Munk (K–M) function, as shown in Fig. S8.† The band gap value calculated by the first-principles calculation is generally smaller than the band gap value calculated by the UV-visible diffuse reflection experiment, which is consistent with our results.

To obtain further insight into changes in the electronic structure, we analyzed the density of states (DOS) of the $ALaLiTeO_6$ (A = Ca, Sr and Ba), as shown in Fig. 5 and Fig. S7 and S9.† For the monoclinic $CaLaLiTeO_6$, the s orbitals and p orbital show dominant contribution near the Fermi level, which is composed of Te-5s/Li-1s hybridized with O 2p orbitals.Te 5s states are completely empty lying 3 eV above the Fermi level in the conduction band, indicating that the electron density of the undoped sample is concentrated in the $[TeO_6]$ eight-coordinated dodecahedron, while the La-5d states are completely filled or empty. With the introduction of rare earth element Yb at the La site, the corresponding s/p/d orbital contribution does not change significantly, but the Yb 4f orbital appears at the Fermi level,[47] and due to the relatively large absorption cross-section, introducing Yb and Tm ion can effectively improve the luminescence properties of the sample. The similar density of states characteristics also appears in $SrLaLiTeO_6$:Yb and $BaLaLiTeO_6$:Yb. After Yb and Tm co-doping in $ALaLiTeO_6$, it can be observed that the valence band (VBM) of $ALaLiTeO_6$:Yb,Tm is composed of the 4f state of Yb and Tm atoms and the 2p state of O atoms. The CBM moves slightly towards the Fermi level, and the main contribution state still comes from the Te-5s state and O 2p, Ca/Sr/Ba/La d states lie far above the Fermi level, which is consistent with the nominal $Ca^{2+}/Sr^{2+}/Ba^{2+}/La^{3+}$ valence state. It is noted that the intensity of the f electrons near the Fermi level significantly increases in the PDOS of $CaLaLiTeO_6$:Yb,Tm and $SrLaLiTeO_6$:Yb,Tm, while the contribution value of the 4f orbital in of the $BaLaLiTeO_6$:Yb,Tm has not increased significantly. The calculation results are consistent with the experimental results that the luminescence intensity of $ALaLiTeO_6$ (Ca, Sr and Ba): Yb, Tm gradually decreases with the change of substituted cations Ca, Sr, and Ba.

3.4 Temperature sensing properties of $ALaLiTeO_6$:5% Yb^{3+},0.2%Tm^{3+}

Under 980 nm excitation, the temperature-dependent spectra of $ALaLiTeO_6$:5%Yb^{3+},0.2%Tm^{3+} (Ca, Sr and Ba) ranging from 303 to 693 K were measured and presented in Fig. 6(a, c and e). A series of emission peaks located at around 450, 475, 649 and 694 nm can be distinguished, which can be assigned to transitions of $^1D_2 \rightarrow {}^3F_4$ (450 nm), $^1G_4 \rightarrow {}^3H_6$ (475 nm), $^1G_4 \rightarrow {}^3F_4$ (649 nm), $^3F_{2,3} \rightarrow {}^3H_6$(694 nm), respectively. However, the response of different radiation transition intensities to temperature changes exhibits different or even opposite trends. The emission intensity generated by $^1D_2 \rightarrow {}^3F_4$ (455 nm), $^1G_4 \rightarrow {}^3H_6$ and $^1G_4 \rightarrow {}^3F_4$ (475 nm and 649 nm: CET from Yb^{3+} ions and ET from $Yb^{3+} \rightarrow Tm^{3+}$ ions) continue to decrease with the rising of temperature. In contrast, the emission intensity gen-

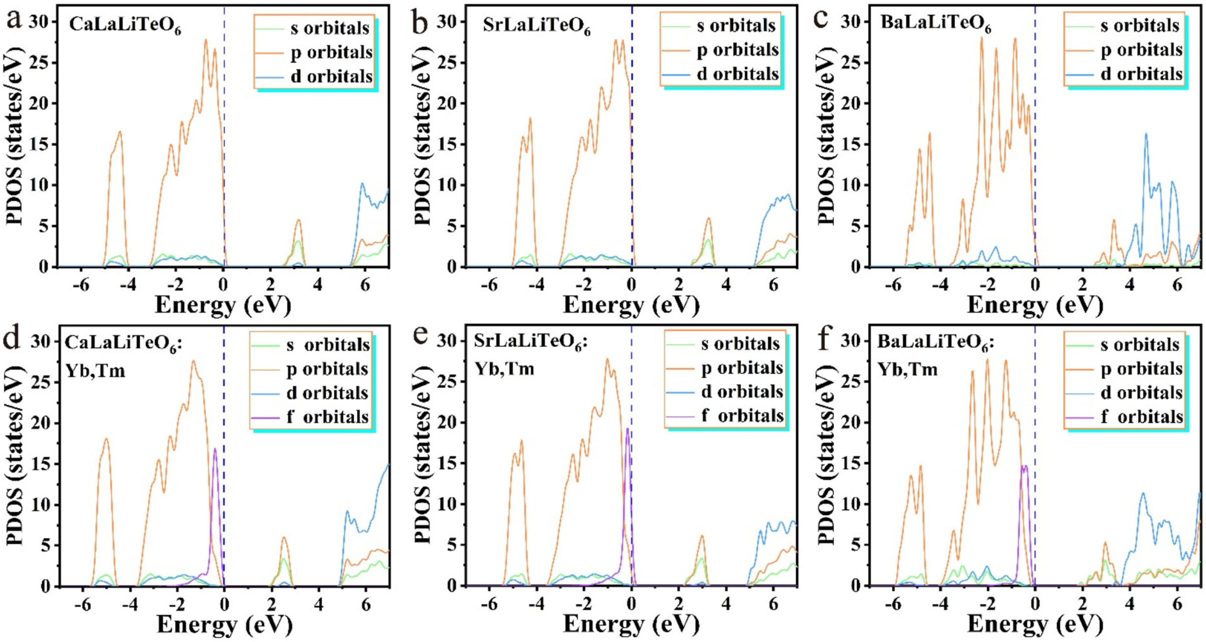

Fig. 5 The PDOS, bonding and anti-bonding orbitals of (a–c) $ALaLiTeO_6$ and (d–f) $ALaLiTeO_6$:Yb,Tm with (A = Ca, Sr, and Ba).

erated by $^3F_{2,3} \rightarrow {}^3H_6$ (694 nm: ET from $Yb^{3+} \rightarrow Tm^{3+}$ ions) increases with the temperature over a certain temperature range.

Considering that the response of fluorescence intensity at 694 nm to temperature changes is completely different from the radiation at 475 nm and 649 nm, we use the fluorescence intensity ratios of $FIR_1 = I_{694}/I_{649}$ and $FIR_2 = I_{694}/I_{475}$ as dual-mode thermometry, respectively. The NTCL with an energy interval greater than 2000 cm^{-1}, and its fluorescence intensity ratio changes with temperature, which does not conform to the Boltzmann distribution.[48] From Table S5,† it can be seen that the energy gap difference of the emission energy levels of Tm^{3+} at 475 nm, 649 nm and 694 nm is about 6500cm^{-1}, since they have a large energy gap difference, this is a non-thermally coupled level, it is difficult to fill them through thermal activation. According to previous reports,[49] one knows that the relation between temperature and FIR values of emissions originating from nonthermally coupled levels can be expressed as:

$$\mathrm{FIR} = A\exp\left(-\frac{B}{T}\right) + C \tag{4}$$

where T is the absolute temperature and A, B and C are fitting constants. The calculated results of FIR in Fig. 6(b, d and f) indicate that FIR highly fits eqn (8). The calculated correlation coefficients R of linear curve fitting are all above 99.7%.

In order to facilitate the evaluation of the fluorescence thermal sensitivity characteristics of materials, two important parameters, absolute sensitivity (S_a) and relative sensitivity (S_r), are usually introduced to compare the temperature measurement accuracy between different thermometers. The calculation formulas for S_a and S_r are as follows:[50,51]

$$S_a = \frac{\mathrm{dFIR}}{\mathrm{d}T} = A\exp\left(-\frac{B}{T}\right) \times \left(\frac{B}{T^2}\right) \tag{5}$$

$$S_r = \frac{1}{\mathrm{FIR}}\frac{\mathrm{dFIR}}{\mathrm{d}T} = \frac{A\exp-\dfrac{B}{T}}{A\exp-\dfrac{B}{T}+C} \times \frac{B}{T^2} \times 100\% \tag{6}$$

The calculated S_a and S_r values of the three UC phosphors in the two temperature measurement modes FIR_1 and FIR_2 are shown in Fig. 7.

The crystal structure distortion of the matrix induced by the change in the ion radius of the A-site has a greater impact on the thermometry performance of the $ALaLiTeO_6$:5%Yb^{3+},0.2% Tm^{3+} phosphor. As shown in Fig. 7a–d, the values of S_a continue to increase as the temperature rises. As the radius of the A-site ion in the matrix crystal $ALaLiTeO_6$ increases, the slope of the increase in the S_a value with increasing temperature continuously increases. Therefore, in the $BaLaLiTeO_6$:5% Yb^{3+},0.2%Tm^{3+} system, under the FIR_1 temperature measurement mode, we calculated the maximum value of S_a to be 10.05% K^{-1} (693 K). In the FIR_1 thermometry mode, the S_r of $CaLaLiTeO_6$ and $SrLaLiTeO_6$ phosphors decreases as the temperature increases. In the FIR_2 thermometry mode, the S_r values of the three phosphors showed a trend of rising first and then falling as the temperature increased. The maximum S_r value of 4.69% K^{-1} (303 K) can be achieved with $SrLaLiTeO_6$:5% Yb^{3+},0.2%Tm^{3+} in the FIR_1 thermometry mode. $ALaLiTeO_6$: Yb^{3+},Tm^{3+} (A = Ca, Sr, Ba) exhibits excellent thermometry sensitivity in both FIR_1 and FIR_2 temperature measurement

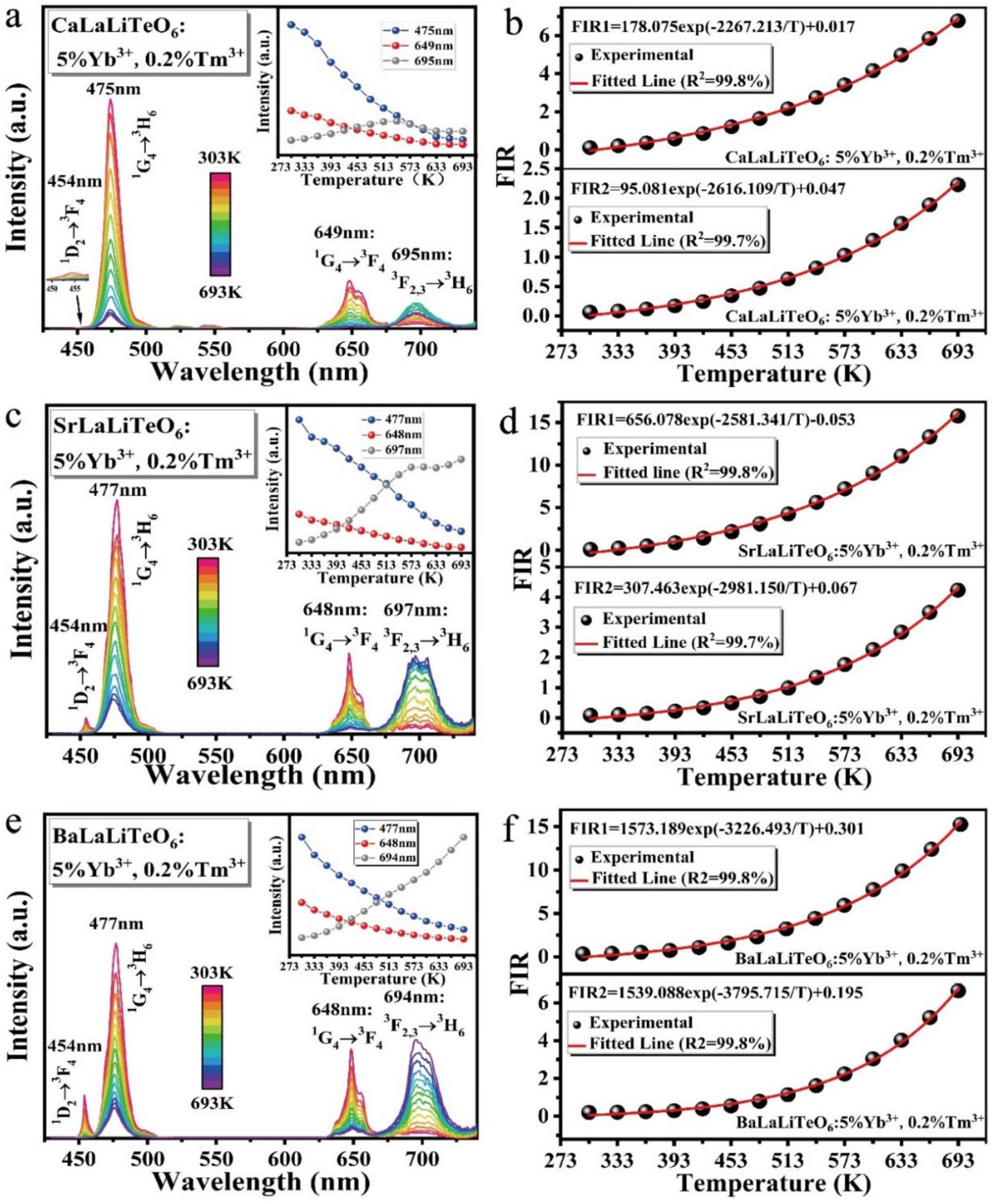

Fig. 6 (a, c and e) The temperature-dependent PL spectra of ALaLiTeO$_6$:5%Yb^{3+},0.2%Tm^{3+} phosphors (inset: the PL emission intensity *versus* various temperatures). (b, d and f) The calculated temperature-dependent fluorescence intensity ratios of FIR$_1$ = ($^3F_{2,3} \rightarrow {}^3H_6$)/($^1G_4 \rightarrow {}^3F_4$) and FIR$_2$ = ($^3F_{2,3} \rightarrow {}^3H_6$)/($^1G_4 \rightarrow {}^3H_6$).

modes. Moreover, the presence of two high sensitivity temperature measurement modes FIR$_1$ and FIR$_2$ can construct a self-calibrating thermometer, further improving the accuracy of temperature monitoring.

The origin of the high-sensitivity optical thermometry of ALaLiTeO$_6$:5%Yb^{3+},0.2%Tm^{3+} is related to the significant difference in the response of the transition emission intensity of the three-photon process and the two-photon process to temperature changes. The emission intensities of 475, 649 and 694 nm are mostly determined by the collaborative action of two non-radiative transitions (NR1: $^3H_5 \rightarrow {}^3F_4$ and NR2: $^3H_5 \rightarrow {}^3F_4$) and three cross-relaxation processes (CR1: $^3H_4 + {}^1G_4 \rightarrow {}^1D_2 + {}^3F_4$, CR2: $^3H_4 + {}^1G_4 \rightarrow {}^3F_4 + {}^1D_2$, CR3: $^3H_6 + {}^1G_4 \rightarrow {}^3F_4 + {}^3F_{2,3}$).[45,52–54] However, it should be noted that the occurrence probability of these two non-radiative transition processes and three cross relaxation processes highly depends on the phonon energy of the matrix crystal. At room temperature, the UC luminescence is mainly affected by multi-phonon-assisted non-radiative transition processes of NR1 and NR2, while the cross-relaxation process probably has little effect on the up-conversion luminescence process. As the temperature increases, the three cross-relaxation (CR1, CR2 and CR3) processes may readily take place with phonon-assistance due to a small energy mismatch (about 590 cm^{-1} for CR1, 290 cm^{-1} for

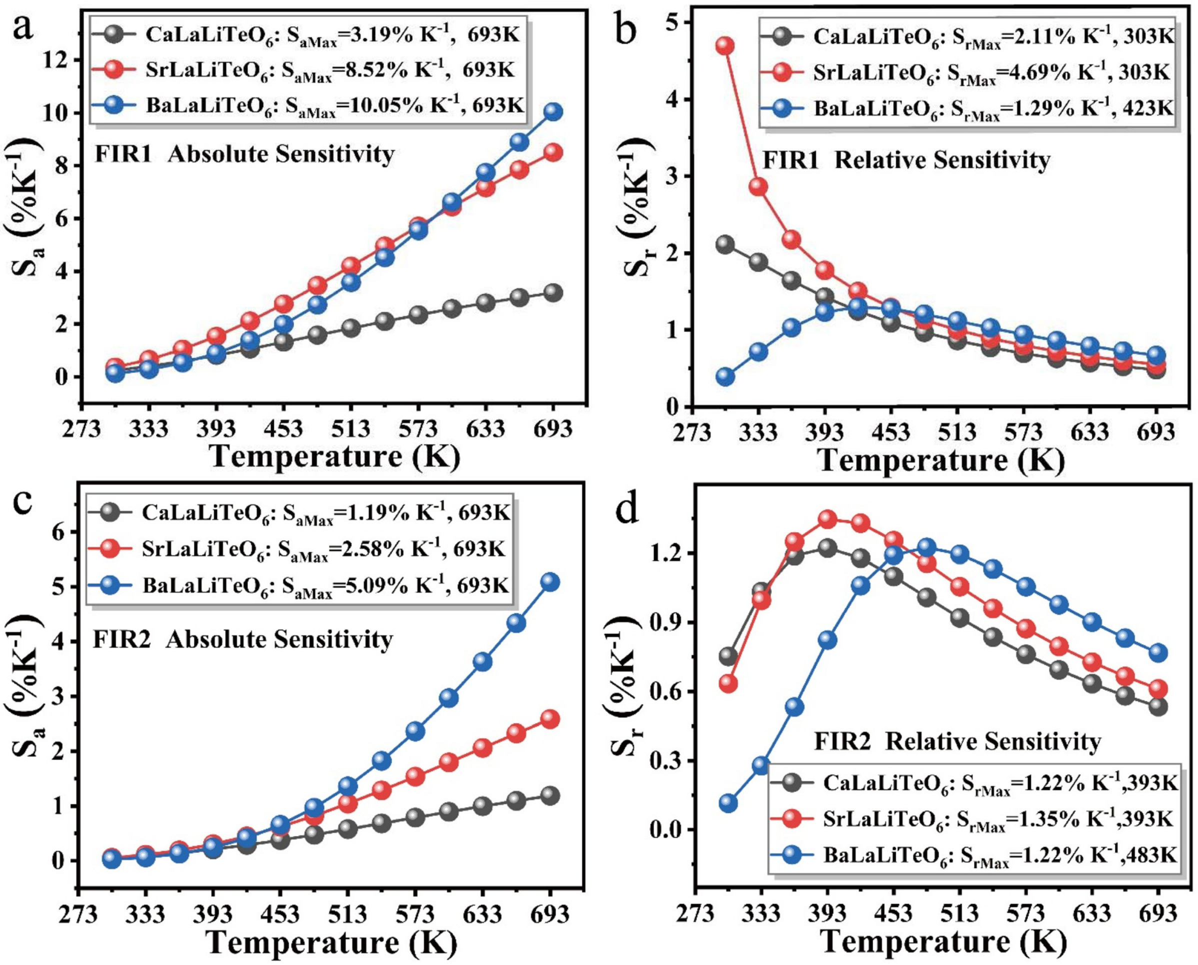

Fig. 7 (a and b) The calculated S_a and S_r values of ALaLiTeO$_6$:Yb^{3+},Tm^{3+} based on FIR$_1$. (c and d) The calculated S_a and S_r values of ALaLiTeO$_6$:Yb^{3+}, Tm^{3+} based on FIR$_2$.

CR2 and 730–1230 cm^{-1} for CR3). Coincidentally, by replacing A-site ions in the matrix crystal of ALaLiTeO$_6$, we effectively regulate the phonon energy, which can better match the energy difference in the Tm^{3+}–Tm^{3+} cross relaxation process, thereby enhancing the occurrence of the three cross relaxation processes of CR1, CR2 and CR3. In the ALaLiTeO$_6$:5% Yb^{3+},0.2%Tm^{3+} system, the increase of temperature will further intensify the lattice vibration of the matrix, and thus enhance the Tm^{3+}–Tm^{3+} phonon-assisted cross relaxation process.

As shown in Fig. 3c, the enhancement of the three phonon-assisted cross relaxation processes CR1, CR2 and CR3 will reduce the population of particles in the $^1G_4$ level, thereby weakening the transition emission intensity of the three-photon process (475 nm and 649 nm). In contrast, the enhancement of the CR3 cross relaxation process can directly increase the population of particles in $^3F_{2,3}$ level, thereby strengthening the emission intensity of the two-photon process (694 nm).

On this basis, we compared the thermometry performances of ALaLiTeO$_6$:5%Yb^{3+},0.2%Tm^{3+} with other published Yb^{3+} and Tm^{3+} co-doped phosphors, as shown in Table S6† and Fig. 8. For the Yb–Tm co-doped system, the fluorescence intensity ratios of 694 nm/649 nm, 694 nm/475 nm, and 694 nm/800 nm were mainly selected as optical temperature measurement energy level pairs. And among them, the optical temperature measurement method based on FIR = 694 nm/649 nm normally exhibits a large S_a but a small S_r value. While the optical thermometers constructed by FIR = 694 nm/475 nm and FIR = 694 nm/800 nm usually demonstrate a large S_r but a small S_a value. It is worth noting that in this work, the optical thermometers constructed based on FIR = 694 nm/649 nm in ALaLiTeO$_6$:5%Yb^{3+},0.2%Tm^{3+} phosphors exhibit significant S_a and S_r values simultaneously. In particular, as the core metric of optical thermometry, the obtained maximum S_r value is much higher than previously reported results. It can be foreseen that Yb^{3+} and Tm^{3+} co-doped ALaLiTeO$_6$ phosphors have broad prospects in temperature detection.

3.5. Repeatability and stability of optical thermometry

A good optical thermometer not only possesses high sensitivity, but also has good stability and repeatability. In order to

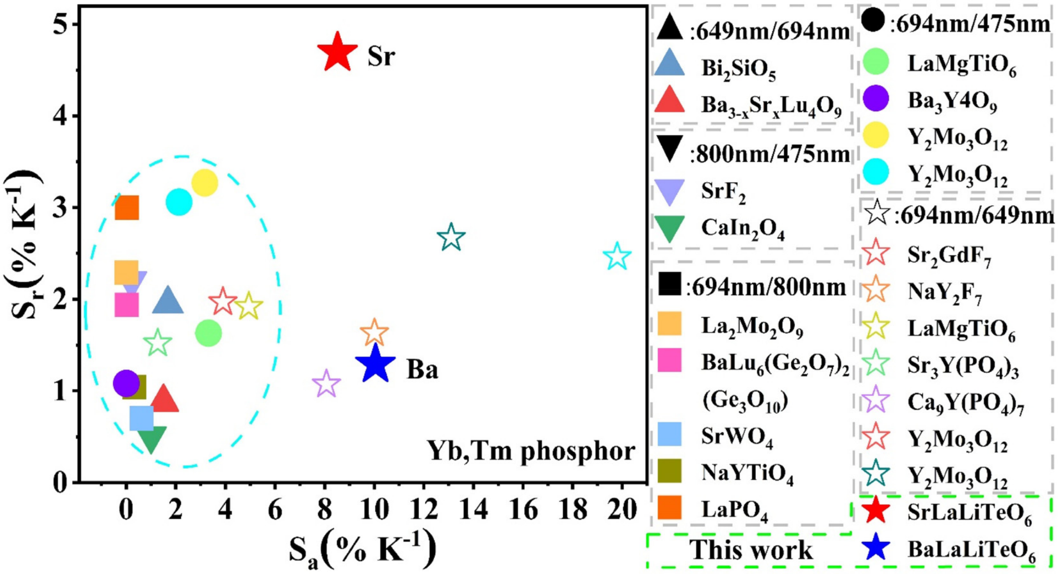

Fig. 8 Comparison of thermometry sensitivity between ALaLiTeO$_6$:5%Yb^{3+},0.2%Tm^{3+} and other Yb^{3+} and Tm^{3+} co-doped phosphors.

evaluate the thermometry repeatability, ten-cycle temperature measurements in the range of 303–603 K were carried out in both FIR$_1$ and FIR$_2$ thermometry modes, and the results are shown in Fig. S10.† Repeatability (R) can be defined as:[55]

$$R = 1 - \frac{\max \mathrm{FIR_C\text{-}FIR_i}}{\mathrm{FIR_C}} \tag{7}$$

where FIR$_\mathrm{i}$ and FIR$_\mathrm{C}$ are the measured and mean values, respectively. It can be seen from Fig. S10† and c that the repetition rates of the three synthesized phosphors for each thermometry mode exceed 97%.

In addition, we continuously measured the FIR spectra of ALaLiTeO$_6$:5%Yb^{3+},0.2%Tm^{3+} in two optical thermometry modes 50 times at an ambient temperature of 603 K, and the measurement results are shown in Fig. 9a and b. On this basis, we calculated the temperature uncertainty (δT) using the following formula:[56]

$$\delta T = \frac{1}{S_\mathrm{r}}\frac{\delta \mathrm{FIR}}{\mathrm{FIR}} \tag{8}$$

where δFIR and FIR are the standard deviation and average value of 50 measurements, respectively. The curve of the variation of δT values with temperature changes obtained from eqn (8) is shown in Fig. S11.† In the temperature range of 303–603 K, the δT values of the ALaLiTeO$_6$:0.2%Tm^{3+},5%Yb^{3+} phosphor was determined to be about 0.283–0.858 K in the optical thermometry FIR$_1$ mode and about 0.479–0.803 K in the optical thermometry FIR$_2$ mode. Low δT values and high R values of the ALaLiTeO$_6$:0.2%Tm^{3+},5%Yb^{3+} phosphor indicate that the two temperature measurement modes constructed

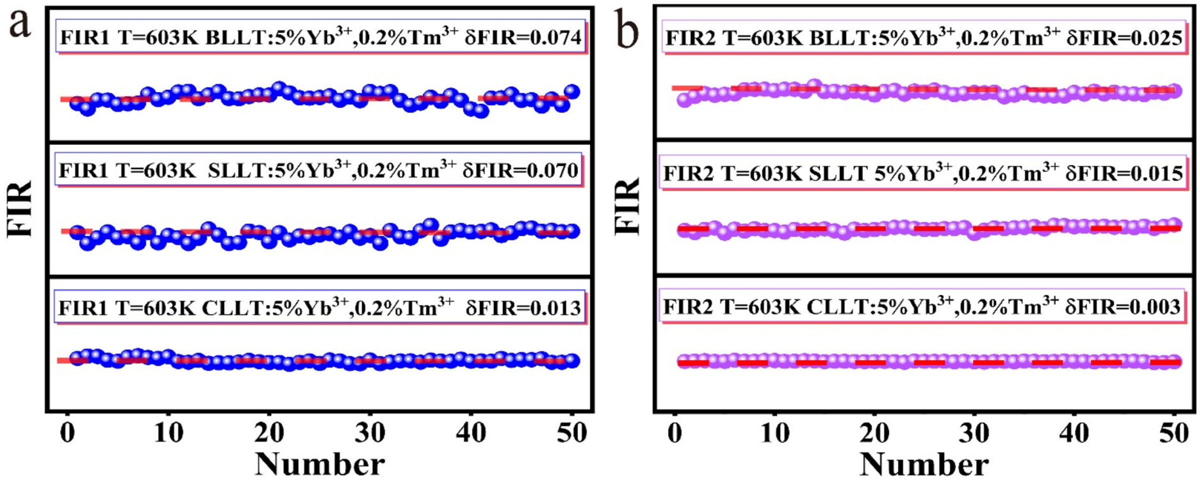

Fig. 9 (a and b) FIR distribution at 603 K for 50 consecutive measurements.

have excellent thermometry sensitivity, stability, and repeatability, making them optical thermometers with great potential for application.

4. Conclusions

We successfully prepared a type of UC phosphor of ALaLiTeO$_6$:5%Yb^{3+},0.2%Tm^{3+} (A = Ca, Sr, and Ba) through a high-temperature solid-state reaction. Based on first principles calculations and combined with XRD and Raman spectroscopy measurements, it has been confirmed that replacing the A-site ions in ALaLiTeO$_6$:5%Yb^{3+},0.2%Tm^{3+} phosphors with Ca^{2+}, Sr^{2+} and Ba^{2+} can effectively regulate the phonon energy of the matrix crystal. The measurement results of temperature-dependent UC emission spectra demonstrate that there is a significant difference in the responses of three photon UC emission (649 and 475 nm) and two-photon UC emission (694 nm) to temperature changes. Therefore, a dual-mode thermometer based on FIR$_1$ = I_{694}/I_{649} and FIR$_2$ = I_{694}/I_{475} was constructed. The maximum S_r = 4.69% K^{-1} (303 K) is achieved in SrLaLiTeO$_6$, while the maximum S_a = 10.05% K^{-1} (693 K) is obtained in BaLaLiTeO$_6$. The origin of high-sensitivity optical thermometry is related to the phonon-assisted cross-relaxation channels of CR1, CR2, and CR3 exhibiting varying degrees of responses to temperature changes. With temperature increases, involving appropriate phonon cooperation, the collaborative action of two non-radiative transitions and three cross-relaxation processes can degrade the emission intensity at 475 nm, but enhance the emission intensity at 694 nm, thus effectively improving the thermometry sensitivity. In addition, the low δT value and high R value indicate that the ALaLiTeO$_6$:5%Yb^{3+},0.2%Tm^{3+} phosphors have excellent thermometry stability and repeatability. Our results not only help construct a highly sensitive optical thermometer, but also provide new insights for exploring ultra-sensitive optical temperature sensors.

Conflicts of interest

There are no conflicts to declare.

Acknowledgements

Financial support from the Key Projects of the Joint Fund for Regional Innovation and Development of the National Natural Science Foundation of China (No. U22A20123), the National Natural Science Foundation of China (Grant's No. 51972181), the Natural Science Foundation of Shandong Province (ZR2021MA008), the High Quality Course Construction Project of Graduate Education in Shandong Province (SDYKC18051) and the Postgraduate Tutor Ability Improvement Project of Shandong Province (SDYY17179) is gratefully acknowledged.

References

1 G. Li, X. Chen, M. Wang, S. Cheng, D. Yang, D. Wu, Y. Han, M. Jia, X. Li, Y. Zhang, C. Shan and Z. Shi, Regulating Exciton De–Trapping of Te^{4+}–Doped Zero–Dimensional Scandium–Halide Perovskite for Fluorescence Thermometry with Record High Time–Resolved Thermal Sensitivity, *Adv. Mater.*, 2023, **35**, 2305495.

2 K. Wu, E. Wang, J. Yuan, J. Zuo, D. Zhou, H. Zhao, Y. Luo, L. Zhang, B. Li, J. Zhang, L. Tu and H. Zhang, Cross Relaxation Channel Tailored Temperature Response in Er^{3+}–rich Upconversion Nanophosphor, *Angew. Chem., Int. Ed.*, 2023, **62**, e202306585.

3 H. Suo, D. Guo, P. Zhao, X. Zhang, Y. Wang, W. Zheng, P. Li, T. Yin, L. Guan, Z. Wang and F. Wang, Ultrasensitive Colorimetric Luminescence Thermometry by Progressive Phase Transition, *Adv. Sci.*, 2024, **11**, 2305241.

4 W. Xu, X. Gao, L. Zheng, Z. Zhang and W. Cao, An optical temperature sensor based on the upconversion luminescence from Tm^{3+}/Yb^{3+} codoped oxyfluoride glass ceramic, *Sens. Actuators, B*, 2012, **173**, 250–253.

5 X. X. Guo, J. H. Wei, J. B. Luo, Z. L. He, Z. Z. Zhang, J. H. Chen and D. B. Kuang, All Inorganic Sb^{3+}–Ln^{3+}–Codoped Cs$_2$NaYCl$_6$ for Highly Efficient Single–Source White–Light Emission and Ratiometric Optical Thermometer Applications, *Adv. Opt. Mater.*, 2023, 2301914, DOI: **10.1002/adom.202301914**.

6 Z. Fan, X. Fan, J. Xue and Y. Wang, Designing dual mode of non-contact optical thermometers in double perovskite Ca2LaTaO6:Bi^{3+}, Eu^{3+} phosphors, *Mater. Today Chem.*, 2023, **30**, 101528.

7 Z. Zeng, B. Huang, X. Wang, L. Lu, Q. Lu, M. Sun, T. Wu, T. Ma, J. Xu, Y. Xu, S. Wang, Y. Du and C. H. Yan, Multimodal Luminescent Yb^{3+}/Er^{3+}/Bi^{3+}–Doped Perovskite Single Crystals for X–ray Detection and Anti–Counterfeiting, *Adv. Mater.*, 2020, **32**, 2004506.

8 Y. Wang, P. Dang, L. Qiu, G. Zhang, D. Liu, Y. Wei, H. Lian, G. Li, Z. Cheng and J. Lin, Multimode Luminescence Tailoring and Improvement of Cs$_2$NaHoCl$_6$ Cryolite Crystals via Sb^{3+}/Yb^{3+} Alloying for Versatile Photoelectric Applications, *Angew. Chem., Int. Ed.*, 2023, **62**, 202311699.

9 H. Suo, X. Zhao, Z. Zhang, Y. Wang, J. Sun, M. Jin and C. Guo, Rational Design of Ratiometric Luminescence Thermometry Based on Thermally Coupled Levels for Bioapplications, *Laser Photonics Rev.*, 2020, **15**, 2000319.

10 Y. Jiang, Y. Tong, S. Chen, W. Zhang, F. Hu, R. Wei and H. Guo, A three-mode self-referenced optical thermometry based on up-conversion luminescence of Ca$_2$MgWO$_6$:Er^{3+}, Yb^{3+} phosphors, *Chem. Eng. J.*, 2021, **413**, 127470.

11 H. Lv, P. Du, W. Li and L. Luo, Tailoring of Upconversion Emission in Tm^{3+}/Yb^{3+}-Codoped Y$_2$Mo$_3$O$_{12}$ Submicron Particles Via Thermal Stimulation Engineering for Non-invasive Thermometry, *ACS Sustainable Chem. Eng.*, 2022, **10**, 2450–2460.

12 C. Wang, H. Zhang, Y. Cai, Q. Wang, B. Zhou, X. Xu and X. Yu, Phonon–Assisted Negative Thermal Quenching in a

One–Photon Up–Conversion Phosphor for Thermometry, *Laser Photonics Rev.*, 2023, **17**, 2300499.

13 K. Zhu, H. Xu, Z. Wang and Z. Fu, Lanthanide-doped lead-free double perovskite La_2MgTiO_6 as ultra-bright multicolour LEDs and novel self-calibrating partition optical thermometer, *Inorg. Chem. Front.*, 2023, 3383–3395, DOI: **10.1039/d3qi00529a**.

14 Q. Zhang, G. Li, G. Li, D. Liu, P. Dang, L. Qiu, H. Lian, M. S. Molokeev and J. Lin, Optical Thermometer Based on Efficient Near–Infrared Dual–Emission of Cr^{3+} and Ni^{2+} in Magnetoplumbite Structure, *Adv. Opt. Mater.*, 2023, 2301429, DOI: **10.1002/adom.202301429**.

15 A. Kabański, M. Ptak and D. Stefańska, Metal–Organic Framework Optical Thermometer Based on Cr^{3+} Ion Luminescence, *ACS Appl. Mater. Interfaces*, 2023, **15**, 7074–7082.

16 D.-H. Chen, R. Haldar and C. Wöll, Stacking Lanthanide-MOF Thin Films to Yield Highly Sensitive Optical Thermometers, *ACS Appl. Mater. Interfaces*, 2023, **15**, 19665–19671.

17 Z. Lei, R. Liu, L. Sun, X. Wang, C. Hu, Y. Zou, X. Yang, S. Su, B. Teng, H. Xu and D. Zhong, An up-conversion $Ba_3In(PO_4)_3$:Er^{3+}/Yb^{3+} phosphor that enables multi-mode temperature measurements and wide-gamut 'temperature mapping', *Dalton Trans.*, 2023, **52**, 10155–10164.

18 Z. Lei, H. Dong, L. Sun, B. Teng, Y. Zou and D. Zhong, Eulytite-type $Ba_3Yb(PO_4)_3$:Tm/Er/Ho as a high sensitivity optical thermometer over a broad temperature range, *J. Mater. Chem. C*, 2024, **12**, 628–638.

19 Y. Zhuang, D. Chen, W. Chen, W. Zhang, X. Su, R. Deng, Z. An, H. Chen and R.-J. Xie, X-ray-charged bright persistent luminescence in $NaYF_4$:Ln^{3+}@$NaYF_4$ nanoparticles for multidimensional optical information storage, *Light: Sci. Appl.*, 2021, **10**, 8670.

20 G. S. Yi and G. M. Chow, Synthesis of Hexagonal–Phase $NaYF_4$:Yb,Er and $NaYF_4$:Yb,Tm Nanocrystals with Efficient Up–Conversion Fluorescence, *Adv. Funct. Mater.*, 2006, **16**, 2324–2329.

21 G. Xiang, J. Zhang, Z. Hao, X. Zhang, G.-H. Pan, L. Chen, Y. Luo, S. Lü and H. Zhao, Solvothermal synthesis and upconversion properties of about 10 nm orthorhombic LuF_3: Yb^{3+}, Er^{3+} rectangular nanocrystals, *J. Colloid Interface Sci.*, 2015, **459**, 224–229.

22 W. Zhang and H. J. Seo, Luminescence and structure of a novel red-emitting phosphor Eu^{3+}-doped tellurate garnet $Li_3Y_3Te_2O_{12}$, *J. Alloys Compd.*, 2013, **553**, 183–187.

23 E.-J. Popovici, M. Nazarov, L. Muresan, D. Y. Noh, L. B. Tudoran, E. Bica and E. Indrea, Synthesis and characterisation of terbium activated yttrium tantalate phosphor, *J. Alloys Compd.*, 2010, **497**, 201–209.

24 J. Liang, S. Zhao, X. Yuan and Z. Li, A novel double perovskite tellurate Eu^{3+}-doped Sr_2MgTeO_6 red-emitting phosphor with high thermal stability, *Opt. Laser Technol.*, 2018, **101**, 451–456.

25 H. Li, H. K. Yang, B. K. Moon, B. C. Choi, J. H. Jeong, K. Jang, H. S. Lee and S. S. Yi, Crystal Structure, Electronic Structure, and Optical and Photoluminescence Properties of Eu(III) Ion-Doped $Lu_6Mo(W)O_{12}$, *Inorg. Chem.*, 2011, **50**, 12522–12530.

26 G. Ahmad, M. B. Dickerson, B. C. Church, Y. Cai, S. E. Jones, R. R. Naik, J. S. King, C. J. Summers, N. Kröger and K. H. Sandhage, Rapid, Room–Temperature Formation of Crystalline Calcium Molybdate Phosphor Microparticles via Peptide–Induced Precipitation, *Adv. Mater.*, 2006, **18**, 1759–1763.

27 Z. Li, X. Ding, H. Cong, S. Wang, B. Yu and Y. Shen, Recent advances on inorganic lanthanide-doped NIR-II fluorescence nanoprobes for bioapplication, *J. Lumin.*, 2020, **228**, 117627.

28 S. Su, C. Hu, S. Ding, Y. Sun, L. Sun, Y. Zou, R. Liu, Z. Lei, B. Teng and D. Zhong, Achieving Broadband NIR Emission in Fe^{3+}–Activated $ALaBB'O_6$ (A = Ba, Sr, Ca; B–B′ = Li–Te, Mg–Sb) Phosphors via Multi–Site Ionic Co–Substitutions, *Adv. Opt. Mater.*, 2023, 2302383, DOI: **10.1002/adom.202302383**.

29 J. Huang, P. Jiang, Z. Cheng, J. Qin, R. Cong and T. Yang, Equivalent chemical substitution in double–double perovskite-type $ALaLiTeO_6$:Mn^{4+} (A = Ba^{2+}, Sr^{2+}, Ca^{2+}) phosphors enabling wide range crystal field strength regulation and efficient far-red emission, *Dalton Trans.*, 2023, **52**, 3458–3471.

30 S. Su, J. Ma, C. Hu, J. Zhao, R. Liu, H. Dong, L. Sun, Y. Zou, Z. Lei, B. Teng and D. Zhong, An efficient double-perovskite $CaLaLiTeO_6$:Mn^{4+} far-red phosphor towards indoor plant lighting application, *J. Alloys Compd.*, 2023, **946**, 169436.

31 R. Phatak, S. K. Gupta, K. Krishnan, S. K. Sali, S. V. Godbole and A. Das, Crystallographic site swapping of La^{3+}ion in $BaA'LaTeO_6$(A′ = Na, K, Rb) double perovskite type compounds: diffraction and photoluminescence evidence for the site swapping, *Dalton Trans.*, 2014, **43**, 3306–3312.

32 B. Amrithakrishnan and G. Subodh, Crystal structure and optical properties of B site-ordered ALaLiTeO6 (A = Ba, Sr) ceramics, *Mater. Res. Bull.*, 2017, **93**, 177–182.

33 S. C. Lal, J. I. Naseemabeevi and S. Ganesanpotti, Deep–red–emitting $SrLaLiTeO_6$: Mn^{4+} double perovskites: Correlation between Mn^{4+}–O^{2-} bonding and photoluminescence, *J. Am. Ceram. Soc.*, 2021, **104**, 5293–5306.

34 J. S. Gong, W. B. Dai, J. Luo, K. Nie and M. Xu, Insights into structure, local site symmetry, and energy transfer for regulating luminescent properties of $SrLaLiTeO_6$: Dy/Eu and its application in wLEDs, *Ceram. Int.*, 2023, **49**, 31024–31034.

35 J. Zhu, T. Yang, H. Li, Y. Xiang, R. Song and H. Zhang, Cationic composition engineering in double perovskite $XLaLiTeO_6$:Eu^{3+}(X = Ba, Sr, Ca, and Mg) toward efficient and thermally stable red luminescence for domestic white-LEDs, *J. Mater. Chem. C*, 2023, **11**, 11017–11026.

36 X. Huang, B. Li and H. Guo, Synthesis, photoluminescence, cathodoluminescence, and thermal properties of novel Tb^{3+}-doped BiOCl green-emitting phosphors, *J. Alloys Compd.*, 2017, **695**, 2773–2780.

37 K. Li, H. Lian, M. Shang and J. Lin, A novel greenish yellow-orange red $Ba_3Y_4O_9$:Bi^{3+},Eu^{3+} phosphor with efficient energy transfer for UV-LEDs, *Dalton Trans.*, 2015, **44**, 20542–20550.

38 X. Ding, Y. Min, C. Wang and Q. Zhang, Near-Infrared Emission Material with Superlong Afterglow Performance and Its Multifunctional Applications, *Inorg. Chem.*, 2023, **62**, 1686–1696.

39 Y. Min, X. Ding, B. Yu, H. Cong and Y. Shen, Rare-earth doped hexagonal $NaYbF_4$ nanoprobes with size-controlled and NIR-II emission for multifunctional applications, *React. Chem. Eng.*, 2023, **8**, 2258–2269.

40 H. Dong, L.-D. Sun and C.-H. Yan, Energy transfer in lanthanide upconversion studies for extended optical applications, *Chem. Soc. Rev.*, 2015, **44**, 1608–1634.

41 M. M. Upadhyay, K. Shwetabh and K. Kumar, Comparative studies of upconversion luminescence and optical temperature sensing in Tm^{3+}/Yb^{3+} codoped $LaVO_4$ and $GdVO_4$ phosphors, *RSC Adv.*, 2023, **13**, 20674–20683.

42 K. Shwetabh, A. Banerjee, R. Poddar and K. Kumar, PEG-coated $NaYF_4$:Tm^{3+}/Yb^{3+} upconversion nanoparticles for OCT image contrast enhancer, optical thermometry, and security applications, *J. Alloys Compd.*, 2024, **980**, 173493.

43 A. Yin, Y. Zhang, L. Sun and C. Yan, Colloidal synthesis and blue based multicolor upconversion emissions of size and composition controlled monodisperse hexagonal $NaYF_4$:Yb,Tm nanocrystals, *Nanoscale*, 2010, **2**, 953.

44 H. Zhang, Y. Fan, P. Pei, C. Sun, L. Lu and F. Zhang, Tm^{3+}–Sensitized NIR–II Fluorescent Nanocrystals for In Vivo Information Storage and Decoding, *Angew. Chem., Int. Ed.*, 2019, **58**, 10153–10157.

45 W. Wei, Y. Zhang, R. Chen, J. Goggi, N. Ren, L. Huang, K. K. Bhakoo, H. Sun and T. T. Y. Tan, Cross Relaxation Induced Pure Red Upconversion in Activator- and Sensitizer-Rich Lanthanide Nanoparticles, *Chem. Mater.*, 2014, **26**, 5183–5186.

46 M. L. López, I. Alvarez, M. Gaitán, A. Jerez, C. Pico and M. L. Veiga, Structural study and magnetic measurements of some perovskites $MLnLiTeO_6$, *Solid State Ionics*, 1993, **63**, 599–602.

47 M. Rathaiah, P. Haritha, A. D. Lozano-Gorrín, P. Babu, C. K. Jayasankar, U. R. Rodríguez-Mendoza, V. Lavín and V. Venkatramu, Stokes and anti-Stokes luminescence in Tm^{3+}/Yb^{3+}-doped $Lu_3Ga_5O_{12}$ nano-garnets: a study of multipolar interactions and energy transfer dynamics, *Phys. Chem. Chem. Phys.*, 2016, **18**, 14720–14729.

48 N. Rakov, Tm^{3+},Yb^{3+}: Y_2SiO_5 up-conversion phosphors: Exploration of temperature sensing performance by monitoring the luminescence emission, *Phys. B*, 2022, **628**, 413572.

49 H. Yu, W. Su, L. Chen, D. Deng and S. Xu, Excellent temperature sensing characteristics of europium ions self-reduction $Sr_3P_4O_{13}$ phosphors for ratiometric luminescence thermometer, *J. Alloys Compd.*, 2019, **806**, 833–840.

50 Z. Sun, Z. Fu, L. Ma, H. Cao, M. Wang, H. Cao and A. Zhang, Excellent multi-color emission and multi-mode optical ratiometric thermometer in (Ca, Tb, Eu, Sm)Nb_2O_6 phosphors based on wide O^{2-}→Nb^{5+} CTB, *Appl. Surf. Sci.*, 2022, **575**, 151791.

51 P. Du, J. Tang, W. Li and L. Luo, Exploiting the diverse photoluminescence behaviors of $NaLuF_4$:xEu^{3+} nanoparticles and g-C_3N_4 to realize versatile applications in white light-emitting diode and optical thermometer, *Chem. Eng. J.*, 2021, **406**, 127165.

52 Y. Zhang, S. Xu, X. Li, J. Sun, J. Zhang, H. Zheng, H. Zhong, R. Hua, H. Xia and B. Chen, Concentration quenching of blue upconversion luminescence in Tm^{3+}/Yb^{3+} co-doped $Gd_2(WO_4)_3$ phosphors under 980 and 808ánm excitation, *J. Alloys Compd.*, 2017, **709**, 147–157.

53 B. P. Kore, A. Kumar, R. E. Kroon, J. J. Terblans and H. C. Swart, Origin of visible and near IR upconversion in Yb^{3+}-Tm^{3+}-Er^{3+} doped $BaMgF_4$ phosphor through energy transfer and cross-relaxation processes, *Opt. Mater.*, 2020, **99**, 109511.

54 X. F. Wang, X. H. Yan, C. X. Kan, K. L. Ma, Y. Xiao and S. G. Xiao, Enhancement of blue emission in β-$NaYbF_4$:Tm^{3+}/Nd^{3+} nanophosphors synthesized by nonclosed hydrothermal synthesis method, *Appl. Phys. B: Lasers Opt.*, 2010, **101**, 623–629.

55 C. D. S. Brites, S. Balabhadra and L. D. Carlos, Lanthanide–Based Thermometers: At the Cutting–Edge of Luminescence Thermometry, *Adv. Opt. Mater.*, 2018, **7**, 1801239.

56 M. Jia, F. Lin, Z. Sun and Z. Fu, Novel excited-state nanothermometry combining the red-shift of charge-transfer bands and a thermal coupling effect, *Inorg. Chem. Front.*, 2020, **7**, 3932–3937.